

Revealing Nanostructures through Plasmon Polarimetry

Marie-Elena Kleemann,[†] Jan Mertens,[†] Xuezhi Zheng,^{†,‡} Sean Cormier,[†] Vladimir Turek,[†] Felix Benz,[†] Rohit Chikkaraddy,[†] William Deacon,[†] Anna Lombardi,[†] Victor V. Moshchalkov,[‡] Guy A. E. Vandenbosch,[§] and Jeremy J. Baumberg^{*,†}

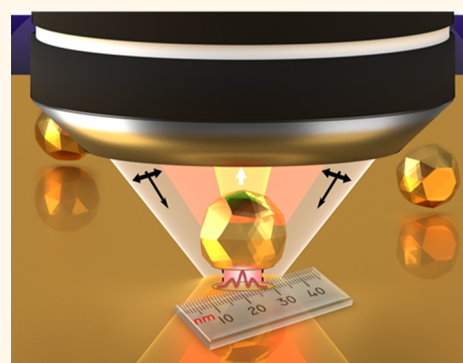
[†]NanoPhotonics Centre, Cavendish Laboratory, University of Cambridge, Cambridge, CB3 0HE, United Kingdom

[‡]Laboratory of Solid State Physics and Magnetism, KU Leuven, Celestijnenlaan 200D, BUS 2414, Leuven 3001, Belgium

[§]Department of Electrical Engineering (ESAT-TELEMIC), KU Leuven, Kasteelpark Arenberg 10, BUS 2444, Leuven 3001, Belgium

S Supporting Information

ABSTRACT: Polarized optical dark-field spectroscopy is shown to be a versatile noninvasive probe of plasmonic structures that trap light to the nanoscale. Clear spectral polarization splittings are found to be directly related to the asymmetric morphology of nanocavities formed between faceted gold nanoparticles and an underlying gold substrate. Both experiment and simulation show the influence of geometry on the coupled system, with spectral shifts $\Delta\lambda = 3$ nm from single atoms. Analytical models allow us to identify the split resonances as transverse cavity modes, tightly confined to the nanogap. The direct correlation of resonance splitting with atomistic morphology allows mapping of subnanometre structures, which is crucial for progress in extreme nano-optics involving chemistry, nanophotonics, and quantum devices.



KEYWORDS: nano-optics, nanoparticles, tunable plasmons, plasmonic cavities, plasmonic polarization signature

Coupled plasmonic structures are of interest due to their extreme light localization and enhanced optical fields as well as their wide tunability. This makes them attractive for surface-enhanced Raman scattering,^{1–4} active optoelectronics,^{5,6} and nanoplasmonic chemistry,⁷ while also making them ideal sensing platforms on the nanoscale.^{8,9} The archetypal plasmonic cavity is formed in an ultrasmall gap between two nanoparticles, but such dimers are hard to manufacture reliably with nanogaps. A more convenient and widely tunable plasmonic coupled system is the “nanoparticle-on-mirror” geometry (NPoM). Image charges induced in an underlying metal film allow plasmonic coupling between a nanoparticle and its mirror image, creating a system that acts as the coupled plasmon dimer. This highly versatile and reproducible construct can be fabricated using self-assembly with high-throughput yields when molecular spacers are used to define the precise gap. Its optical signature, arising from mixing of coupled plasmonic modes in the NPoM system, is very sensitive to the exact gap morphology as well as to the system geometry, allowing the hotspot created in the nanocavity to be directly tuned.

Much work analyzes the influence of nanoparticle size,^{10–12} substrate,¹³ spacer gap size and material,^{14,15} nanoparticle shape,^{16,17} faceting of the nanoparticle and its edge rounding^{18–21} as well as the effect of symmetry and the topology of

dimers/trimers,^{3,22–28} with corresponding extensive theory work.^{19,29–31} Despite wide interest in this field and significant theoretical progress, mapping the exact morphology of plasmonic cavities remains a challenge; the cavity is inaccessible beneath the nanoparticle on top of it. Moreover, commonly used imaging methods such as SEM and TEM that rely on accelerated electrons to image structures damage these constructs and change their optical signatures, thus making the analysis complicated and irreproducible.³²

RESULTS AND DISCUSSION

Here, we demonstrate that noninvasive polarization-dependent broadband dark-field spectroscopy can map out the influence of nanoparticle faceting and asymmetries with nanometer resolution, thus accessing the concealed plasmonic cavity (Figure 1). Employing incident polarizations in the azimuthal plane (xy plane parallel to the substrate Figures 1a and S1) excites tightly confined dark cavity modes that are highly sensitive to the exact morphology of the cavity, controlling the optical response in the near field. Together with boundary element method (BEM) simulations, we reveal the origin of

Received: November 1, 2016

Accepted: December 16, 2016

Published: December 16, 2016

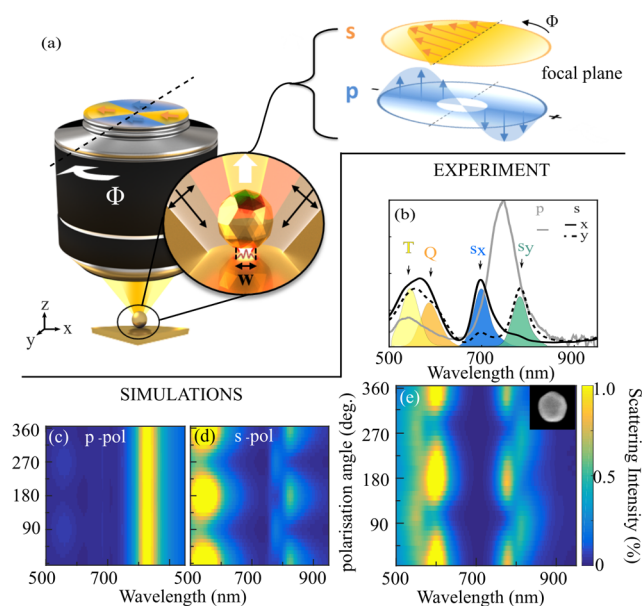


Figure 1. Polarization-dependent dark-field scattering of an 80 nm faceted Au nanoparticle atop a 0.9 nm molecular spacer layer of CB[7] on an Au mirror (NPoM). (a) Schematic of experimental setup with incident light within a cone at high angles. Red line in inset is gap plasmon mode amplitude. Right side shows how linear polarized coherent light transforms into the two different polarizations in the focal plane. (b) Scattering spectra of p-polarized (gray) compared to s-polarized (black) incident light. Orthogonal polarization axes (x , y) within the azimuthal plane (solid, dashed) show different modes. T: transverse, Q: quadrupolar, $s_{x,y}$: dark cavity modes. (c, d) Simulated dark-field scattering from NPoM for p-/s-polarized light. (e) Dark-field scattering spectra vs azimuthal polarization (s-pol input), inset: SEM image.

these modes, exposing the precise geometry and orientation of the facet, which is hidden underneath the nanoparticle. Comparison to an analytical cavity model creates an intuitive picture, advancing our understanding of how atomistic changes in the gap morphology affect the optical response of plasmonic coupled systems with sub-nm separation.

The resonant modes trapped inside the gap between nanoparticle and flat substrate correspond to confined modes of the metal–insulator–metal waveguide (Figure 1a red line). The spacer prevents the formation of a conductive contact, creating an ultrathin cavity between the faceted nanoparticle and the metal film. Using different spacer materials allows for control of its effective refractive index and gap size (down to 0.3 nm),³³ tuning the resulting optical properties. In a simplified model, these modes can be described as drum-like standing waves and calculated analytically to give¹⁸

$$\lambda_i(w, d) = \lambda_p \sqrt{w \varepsilon_d / (d \alpha_i) + \varepsilon_\infty} \quad (1)$$

where λ_p is the plasmon wavelength of Au (~ 148 nm), ε_∞ is the Au background permittivity (~ 10), ε_d is the permittivity of the gap spacer, w is the facet width, d the nanogap size, and α_i is the i -th antinode of the $J_0(\alpha)$ cylindrical Bessel function. These transverse modes depend on facet width and radiate if they have the correct symmetry, because they then couple to a second type of global “antenna” plasmon with a vertical dipole.^{12,19,33} Even-order modes i are found to be bright, while odd-order modes are dark. So far, the bright modes have been

used to track the morphology of nanoparticles³² and their atomic-scale dynamics.^{15,16,18,32}

Rotating the input polarization changes the incident direction of s-pol light in the azimuthal plane, allowing us to excite odd-order modes, which are found to be even more sensitive to morphology than even-order bright modes. A supercontinuum laser in a custom-built dark-field microscope with a high-NA water-immersion objective is used to analyze the far-field scattering (Figure 1a). High-angle $\vartheta = 55^\circ$ – 65° annular excitation produces scattered light from individual NPoMs, collected in a cone from 0° – 55° . The incident light is linearly polarized with a grid polarizer and then rotated by Φ in the azimuthal plane by an ultrabroadband half-wave plate in the excitation beam path (Figure 1a and Supporting Information sections I–III). In contrast to former studies,^{11,14,15,33,35} this leads to purely s-polarized excitation, oscillating parallel to the surface.³⁶ The background-free dark-field scattering is extracted by blocking the incident light with an aperture and spectrally analyzing in confocal detection.

Nanocavities are built using 80 nm gold nanoparticles on gold substrates with a rigid monolayer of cucurbit[7]uril (CB[7]) as the molecular spacer ($d = 0.9$ nm thickness). Conventional dark-field spectroscopy on NPoMs with unpolarized white light probes the vertical antenna mode with p-polarization. These modes show negligible polarization dependence (Figure 1c) due to their z -oriented dipole, which gives a centrosymmetric charge distribution within the gap that is independent of the facet asymmetry.

However, s-polarized incident light yields a distinctively different optical response with polarization angle (Figure 1e). Incident light polarized within the azimuthal plane along the nanocavity excites odd-order transverse modes. We identify three different modes (Figure 1b) besides the single nanoparticle transverse (T) mode at 550 nm. The mode around 607 nm can be identified as a quadrupolar (Q), which is discussed later. Most significant are the two longer wavelength modes labeled $s_{x,y}$ at 787 and 827 nm, which show a clear polarization dependence. Their polarization response is phase-shifted by 90° between the two modes and depends on the deviation from a perfectly spherical nanoparticle (SEM image Figure 1e). This polarization-dependent “splitting” seems counterintuitive because it coincides with the longitudinal-coupled dipolar mode but, as we show, can be explained by comparing the experimental data to simulations.

Full BEM simulations (see Supporting Information section IV) of the faceted nanoparticles use a fixed gap of 0.9 nm and ε_{Au} from ref 37. The experimental conditions are reproduced by exciting the NPoM from azimuthal direction Φ at an incident angle $\vartheta = 55^\circ$ for p-/s-polarizations. For s-coupled light, rotating the input polarization from 0 to 360° in our annular excitation condition corresponds to changing the incident direction (Figure 2a). Different NP structures are simulated to match the resonance positions of the modes in the experimental data. Best agreement is found for a faceted sphere which is slightly elongated along one axis into an ellipsoid, with semimajor axes of $a_x = 30$ nm, $a_y = a_z = 40$ nm, and a facet width of $w_y = 25$ nm. Simulations using this geometry with p- and s-polarized light are shown in (Figure 1c,d) respectively. The spectral map for s-polarization consists of four modes, with peak positions at 545 nm (T), 580 nm (Q), and 780 and 830 nm (s_x , s_y), matching the experimental mode positions well. The quadrature polarization dependence of s_x and s_y modes is also seen in the simulations. To better understand the mode

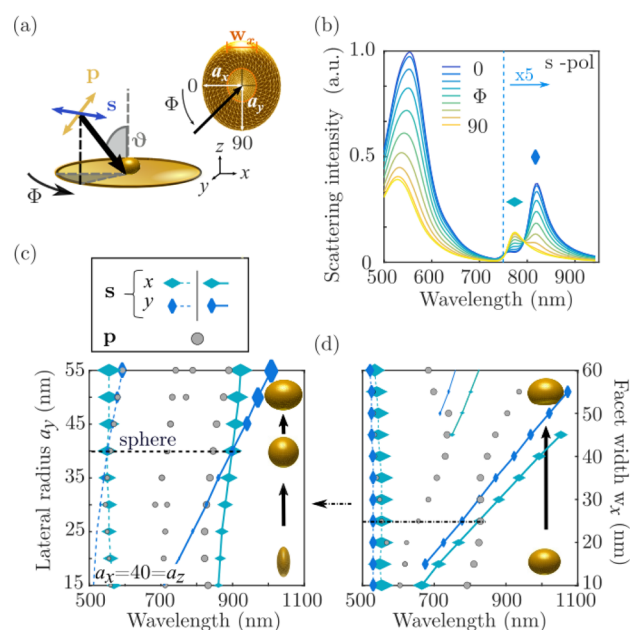


Figure 2. Simulations of NPoM. (a) Simulation setup, ellipsoid semi-axes $a_{x,y}$ and facet widths $w_{x,y}$. (b) Simulated scattering spectra for s-polarized incidence vs azimuthal angle Φ ($\times 5$ for $\lambda > 750$ nm). (c, d) Extracted peak positions (along x: blue, vertical diamond and y: turquoise horizontal diamond) of cavity and antenna modes for (c) changing aspect ratios a_x/a_y of a cropped ellipsoid on mirror with a 25 nm facet width, and (d) changing facet size of a $60 \times 80 \times 80$ nm cropped ellipsoid on mirror. Dashed line indicates facet width in (c). Size of marker points in (c,d) shows the amplitudes of each mode at extracted peak positions.

origins, we explore the symmetry-breaking (Figure 2). Peak positions are extracted from the spectra as the incident angle is rotated around the nanoparticle (Figure 2b).

Distorting the geometry has little effect on the z-polarized hybridized antenna-cavity modes (longitudinal p-modes; gray points Figure 2c), except a small effect on the resonance position as a result of changing nanoparticle size.¹¹ By contrast, exciting with s-polarization for $\Phi = 0^\circ$ (along x, blue, vertical diamond) and 90° (along y, turquoise, horizontal diamond) shows how the modes directly track the facet width in the incident direction. Fixing the 80 nm height of the nanoparticle, but elongating the truncated sphere along the x-direction, shows that the s_y mode depends most on the facet size w_x (Figure 2c, dark blue line). With circular facets, modes $s_{x,y}$ are degenerate (dashed horizontal line), while the s-mode splitting becomes more pronounced for larger asymmetries (with small effects on the Q mode at 580 nm also seen). Increasing the faceting of the nanoparticle while keeping the facet asymmetry fixed (Figure 2d) shows that the relative splitting is preserved (turquoise/blue lines). Changing the incident linear polarization for s-coupled light thus clearly accesses cavity modes along different facet directions. Higher order modes that appear for larger facets ($w_x > 45$ nm) are similarly spectrally split, while without the facet, these cavity modes are suppressed. By contrast, p-modes are polarization independent, but only tune with facet size. Although p-modes depend on nanoparticle size,¹¹ gap size,¹⁵ and average facet width,²¹ they are not sensitive to the exact geometry of the facet and its asymmetry. The polarization dependence is also captured in the charge distributions (Figure 3a). The surface charge indeed depends on the incident direction. While the dipolar p-mode and

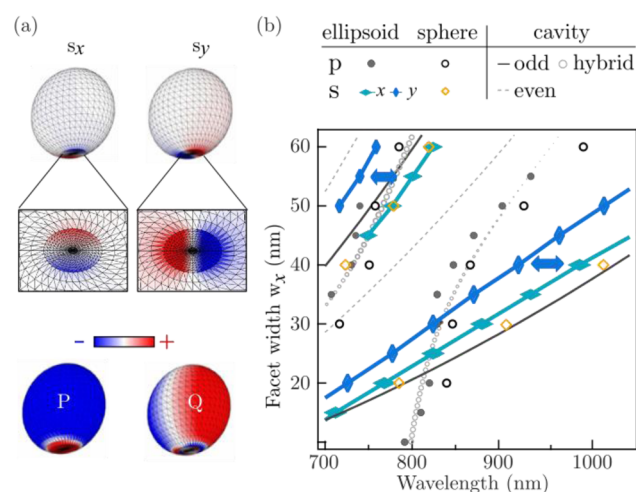


Figure 3. Mode analysis. (a) Simulated surface charge distribution for a slightly ellipsoidal Au NPoM ($a_x = 30$ nm, $a_y = a_z = 40$ nm) on Au substrate with 0.9 nm gap. Top panels show the two gap-confined cavity modes $s_{x,y}$, while bottom panels display radiative dipolar p- and quadrupolar Q-modes. (b) Comparison of analytical cavity model (gray lines, dark solid = odd, dashed = even) and full BEM simulations (blue, orange, and gray points).

quadrupolar Q-mode have surface charges distributed around the entire particle (bottom panels), the $s_{x,y}$ modes are strongly confined to the nanocavity gap (top panels), emphasizing their different origin and character. As anticipated, $s_{x,y}$ modes show charge separation along the two perpendicular axes of the facet, directly relating the polarization splitting to the orientation of the facet. Facet-dependent spectral splitting is seen as the facet diameter increases (Figure 3b, same parameters as before). From the previously discussed model of eq 1, dark odd modes (solid) and bright even modes (dashed) are shown (gray lines) superimposed on the p-modes of the exact simulations for spherical (black, open circle) and ellipsoidal nanoparticles (black, solid circle). The sphere has degenerate s-modes (orange, open square) which match eq 1 extremely well for mode order $i = 1$. This model confirms that s-polarized light is capable of exciting usually dark odd symmetry cavity modes. If the facet is noncircular (including also the cube on mirror geometry), the spectral s-mode positions depend on the effective nanocavity length in the direction of the optical field (the s_x mode has a shorter cavity and thus higher energy compared to the s_y mode, Figure 3a,b).

The simulations imply that s-modes seen in the experiment are tightly confined odd transverse cavity modes. While usually dark because of their symmetry, these modes become bright and can radiate into the far field due to the rounded edges of the nanoparticle and non-normal illumination on the flat mirror, revealing the detailed morphology of the nanocavity. The polarization-dependent mode splitting is only ever two-fold symmetric and maximized for rectangular or elliptic facets. The much stronger out-coupling of p-modes arises from the even-cavity mode coupling to the antenna modes, which results in hybrid modes that anticross (dashed open circles, Figure 3b), as discussed previously.^{18,19} In contrast, the s-modes cannot couple to the antenna mode due to their symmetry and are only weakly emitted. Our analysis allows us to explore the behavior of many different NPoMs, which possess different facet morphologies. We compare the polarization dependent dark-field scattering spectra with the precise particle orientation

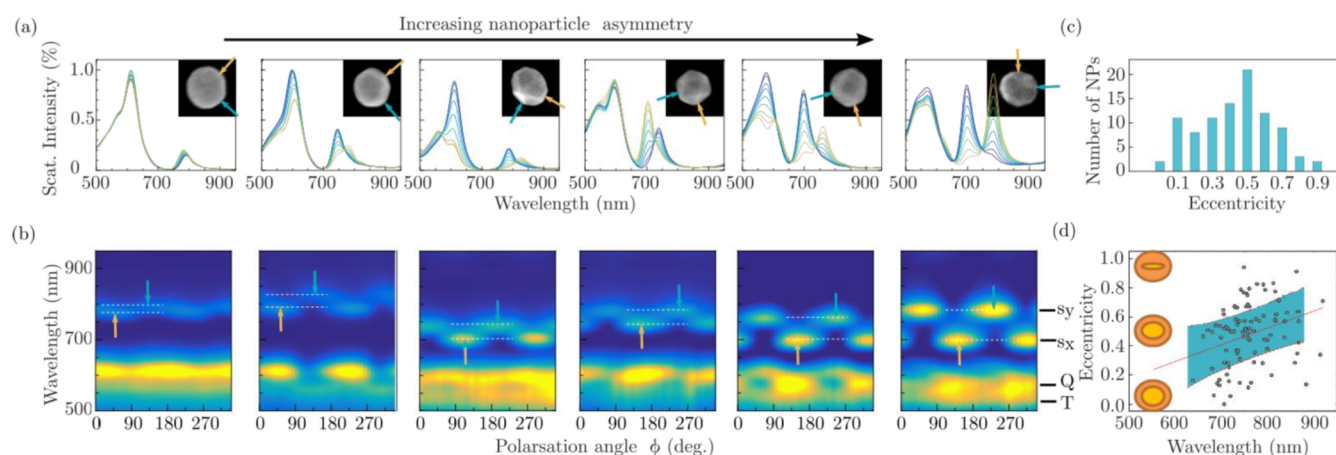


Figure 4. Dependence on nanoparticle shape. (a) Dark-field scattering spectra for 80 nm Au faceted NPoMs correlated with SEM images (insets). Orange and blue arrows in SEMs indicate polarization angle of maximum intensity for the s_x and s_y modes, respectively. (b) Polarization maps, which provide optical orientations (orange and blue arrows), used in (a). Dashed white lines mark the spectral splitting, which increases with growing asymmetry (to the right). (c) Distribution of extracted facet eccentricity for 100 NPs, plotted in (d) vs mean resonance position $\bar{\lambda}_s = 0.5(\lambda_{s_x} + \lambda_{s_y})$.

obtained *via* SEM on exactly the same nanoparticles (Figure 4). The raw polarization-dependent spectra (Figure 4a) show considerable variation in response, which is in agreement with the variety of faceted images obtained from electron microscopy (Figure 4a, insets). The orange and blue arrows in the SEM images and polarization maps (Figure 4b) indicate the polarization angles of the peak maxima for s_x and s_y modes, respectively. The mode spectral separation is indicated with white dashed lines. Strong variation is seen at longer wavelength s -modes. With increasing particle asymmetry in the SEM images (when moving to the right), the spectral mode splitting increases, also agreeing with our simulations. The increased mode splitting is accompanied by increasing scattering strengths and more equal intensities of the two split modes, also agreeing with theory. The splitting is a direct measure of the aspect ratio of the bottom facet, with the eccentricity:

$$e = \sqrt{1 - \frac{w_y}{w_x}} = \sqrt{1 - \frac{\lambda_y^2 - \lambda_p^2 \epsilon_\infty}{\lambda_x^2 - \lambda_p^2 \epsilon_\infty}}$$

The distribution of e_n of 100 NPoMs reveals that virtually all NPs deviate from spheres, giving a polarization splitting (Figure 4d). The average $\bar{e} \sim 0.5$ (Figure 4c) corresponds to elongated NPs with a facet ratio of 2:1 (Figure 4d). The variation in mean resonance position $\bar{\lambda}_s$ (corresponding to average facet width) is positively correlated with the s -mode splitting (and therefore eccentricity e); larger facets are thus more asymmetric. Through the mode splitting, we are able to track morphological changes in the facet ratio down to the single atom level. From BEM simulations, increasing a facet axis by only one atom (with atomic spacing 0.4 nm¹⁸) leads to a spectral splitting of $\Delta\lambda = 3$ nm. Combined p - and s -polarized measurements thus allow precise description of the nanoconstructs. While p -polarized light couples to the antenna mode that is highly sensitive to NP size and gap distance, s -polarized light is able to access detailed information about the size and shape of the facet at the bottom of each Au nanoparticle, giving a polarimetry plasmonic ruler.

A number of details remain puzzling. In particular, the Q -mode intensity is strongest whenever the shortest wavelength s -mode, labeled here s_w , has a strong scattering amplitude (Figure

4b). In simulations, however, the Q -mode aligns spectrally with the longer wavelength s -mode (Figures 1e and 2c). This consistent result shows that an extra mixing is missing in our simple analytical cavity model. However, the general trends and the effectiveness of our analytic model verify the correct origin of the observed polarization splitting.

CONCLUSION

In conclusion, we have shown that polarization-dependent dark-field scattering can be used for noninvasive characterization to probe metallic nanostructures at the subnanometer scale. Within coupled systems, it identifies the asymmetry and orientation of plasmonic nanocavities, which are hidden underneath nanoparticles and which are inaccessible to conventional imaging methods. Polarization splittings in dark-field scattering are directly related to the asymmetry of the gap morphology, accessing dark cavity plasmons, which can be excited due to symmetry breaking. Comparing experimental results on hundreds of NPoMs to simulations and a simple analytical model reveals the origin of these plasmonic coupled modes and demonstrates their tunability, making them ideal candidates for ultrasensitive plasmonic sensing on the nanoscale. Our findings allow for the full optical interrogation of nanocavities essential for their reliable utilization in SERS, quantum plasmonics, nanoscale chemical reactions, and nanoscale rulers.

METHODS

Sample Preparation. Au substrates are fabricated using a template stripping method. A gold layer of 100 nm thickness is electron-beam-evaporated onto a polished Si wafer. Using epoxy glue (EPOTEK377), silicon substrates of approximately 1 cm² are glued to the Au surface and left on a hot plate at 150 °C for 2 h to cure the epoxy. After slowly cooling down, the template stripped Au can be extracted by gently pushing the silicon substrates, leaving an atomically smooth surface of Au adhering to the glue on the small silicon squares. The Au-coated substrates are submerged in a 1 mM solution of CB[7] in deionized water for 1 h to deposit a layer of CB[7] molecules. To form the NPoM geometry, 80 nm citrate-capped Au nanoparticles in solution (BBI) are deposited on top of the CB[7] monolayer, where surface binding takes place. The sample is rinsed with deionized water after 10 s and purged with nitrogen to remove excess particles.

Experimental Spectroscopy. Optical spectroscopy was performed on a custom-built dark-field microscope with a confocal fiber collection arrangement. A supercontinuum Fianium laser with a power density ~ 100 kW/cm² was used in the excitation. Using a beam splitter to couple the laser light into the microscope, the incident light is focused through a Leica high-NA water-immersion objective (63 \times magnification, 1.2 NA), providing an annular ring excitation at 64 $^\circ$ surrounding the collection cone. The input polarization was set with a grid polarizer (GP) and rotated using a broadband zero-order half-wave. Using a beam block in the excitation beam path and an aperture in the detection, background-free dark-field scattering was collected with a cooled ocean optics spectrometer (SI Figure S1). SEM imaging was performed in a Hitachi S-5500 SEM at 30 kV acceleration voltage.

Theoretical Methods. Exact simulations are carried out using the BEM.^{34,35} The algorithm was first proposed in refs 38–40, then extended to the layered media case in ref 41 and adapted with a more efficient multilayer Green's function evaluation, as described in ref 42. In order to ensure converging solutions in all cases, the grids are chosen sufficiently small. The NPoM geometry is simulated using a four-layered system: the Au substrate layer, the CB gap layer, the scatterer (Au ellipsoid), and the surrounding medium (air). The variation of the incident polarization is achieved by rotating the incident angle in p- and s-configurations (see Supporting Information, section IV for more details).

ASSOCIATED CONTENT

Supporting Information

The Supporting Information is available free of charge on the ACS Publications website at DOI: 10.1021/acsnano.6b07350.

Additional experimental details and data (PDF)

AUTHOR INFORMATION

Corresponding Author

*E-mail: jjb12@cam.ac.uk.

ORCID

Jeremy J. Baumberg: 0000-0002-9606-9488

Notes

The authors declare no competing financial interest.

ACKNOWLEDGMENTS

We acknowledge support from EPSRC grant EP/L027151/ERC, grant LINASS 320503, the Winton Programme for the Physics of Sustainability, the CI Taylor Fund, the C2 project (C24/15/015), the PDMK/14/126 project of KU Leuven, the FWO long-term stay abroad project grant V405115N, and the Methusalem project of the Flemish government. R.C. acknowledges support from the Dr. Manmohan Singh scholarship from St John's College, University of Cambridge.

REFERENCES

- (1) Wei, H.; Xu, H. Hot Spots in Different Metal Nanostructures for Plasmon-Enhanced Raman Spectroscopy. *Nanoscale* **2013**, *5*, 10794.
- (2) Ding, T.; Herrmann, L. O.; de Nijs, B.; Benz, F.; Baumberg, J. J. Self-Aligned Colloidal Lithography for Controllable and Tuneable Plasmonic Nanogaps. *Small* **2015**, *11*, 2139.
- (3) Chen, T.; Pourmand, M.; Feizpour, A.; Cushman, B.; Reinhard, B. M. Tailoring Plasmon Coupling in Self-Assembled One-Dimensional Au Nanoparticle Chains through Simultaneous Control of Size and Gap Separation. *J. Phys. Chem. Lett.* **2013**, *4*, 2147.
- (4) Xu, H.; Bjerneld, E. J.; Käll, M.; Börjesson, L. Spectroscopy of Single Hemoglobin Molecules by Surface Enhanced Raman Scattering. *Phys. Rev. Lett.* **1999**, *83*, 4357.
- (5) Large, N.; Abb, M.; Aizpurua, J.; Muskens, O. L. Photoconductively Loaded Plasmonic Nanoantenna as Building Block for Ultracompact Optical Switches. *Nano Lett.* **2010**, *10*, 1741.

- (6) Lumdee, C.; Toroghi, S.; Kik, P. G. Post-Fabrication Voltage Controlled Resonance Tuning of Nanoscale Plasmonic Antennas. *ACS Nano* **2012**, *6*, 6301.

- (7) Baffou, G.; Quidant, R. Nanoplasmonics for Chemistry. *Chem. Soc. Rev.* **2014**, *43*, 3898.

- (8) Novotny, L.; van Hulst, N. Antennas for Light. *Nat. Photonics* **2011**, *5*, 83.

- (9) Anker, J. N.; Hall, W. P.; Lyandres, O.; Shah, N. C.; Zhao, J.; Van Duyne, R. P. Biosensing with Plasmonic Nanosensors. *Nat. Mater.* **2008**, *7*, 442.

- (10) Benz, F.; Chikkaraddy, R.; Salmon, A.; Ohadi, H.; de Nijs, B.; Mertens, J.; Carnegie, C.; Bowman, R. W.; Baumberg, J. J. SERS of Individual Nanoparticles on a Mirror: Size Does Matter, but so Does Shape. *J. Phys. Chem. Lett.* **2016**, *7*, 2264.

- (11) Benz, F.; Tserkezis, C.; Herrmann, L. O.; de Nijs, B.; Sanders, A.; Sigle, D. O.; Pukenas, L.; Evans, S. D.; Aizpurua, J.; Baumberg, J. J. Nanooptics of Molecular-Shunted Plasmonic Nanojunctions. *Nano Lett.* **2015**, *15*, 669.

- (12) Huang, C.-Z.; Wu, M.-J.; Chen, S.-Y. High Order Gap Modes of Film-Coupled Nanospheres. *J. Phys. Chem. C* **2015**, *119*, 13799.

- (13) Chen, S. Y.; Mock, J. J.; Hill, R. T.; Chilkoti, A.; Smith, D. R.; Lazarides, A. A. Gold Nanoparticles on Polarizable Surfaces as Raman Scattering Antennas. *ACS Nano* **2010**, *4*, 6535.

- (14) Lei, D. Y.; Fernandez-Dominguez, A. I.; Sonnefraud, Y.; Appavoo, K.; Haglund, R. F.; Pendry, J. B.; Maier, S. A. Revealing Plasmonic Gap Modes in Particle-on-Film Systems Using Dark-Field Spectroscopy. *ACS Nano* **2012**, *6*, 1380.

- (15) de Nijs, B.; Bowman, R. W.; Herrmann, L. O.; Benz, F.; Barrow, S. J.; Mertens, J.; Sigle, D. O.; Chikkaraddy, R.; Eiden, A.; Ferrari, A.; Scherman, O. A.; Baumberg, J. J. Unfolding the Contents of Sub-Nm Plasmonic Gaps Using Normalising Plasmon Resonance Spectroscopy. *Faraday Discuss.* **2015**, *178*, 185.

- (16) Tong, L.; Wei, H.; Zhang, S.; Li, Z.; Xu, H. Optical Properties of Single Coupled Plasmonic Nanoparticles. *Phys. Chem. Chem. Phys.* **2013**, *15*, 4100–4109.

- (17) Ringe, E.; Sharma, B.; Henry, A.-I.; Marks, L. D.; Van Duyne, R. P. Single Nanoparticle Plasmonics. *Phys. Chem. Chem. Phys.* **2013**, *15*, 4110.

- (18) Sigle, D. O.; Mertens, J.; Herrmann, L. O.; Bowman, R. W.; Ithurria, S.; Dubertret, B.; Shi, Y.; Yang, H. Y.; Tserkezis, C.; Aizpurua, J.; Baumberg, J. J. Monitoring Morphological Changes in 2D Monolayer Semiconductors Using Atom-Thick Plasmonic Nanocavities. *ACS Nano* **2015**, *9*, 825.

- (19) Tserkezis, C.; Esteban, R.; Sigle, D. O.; Mertens, J.; Herrmann, L. O.; Baumberg, J. J.; Aizpurua, J. Hybridization of Plasmonic Antenna and Cavity Modes: Extreme Optics of Nanoparticle-on-Mirror Nanogaps. *Phys. Rev. A: At., Mol., Opt. Phys.* **2015**, *92*, 053811.

- (20) Grillet, N.; Manchon, D.; Bertorelle, F.; Bonnet, C.; Broyer, M.; Cottancin, E.; Lermé, J.; Hillenkamp, M.; Pellarin, M. Plasmon Coupling in Silver Nanocube Dimers: Resonance Splitting Induced by Edge Rounding. *ACS Nano* **2011**, *5*, 9450.

- (21) Mertens, J.; Demetriadou, A.; Bowman, R. W.; Benz, F.; Kleemann, M.-E.; Tserkezis, C.; Shi, Y.; Yang, H. Y.; Hess, O.; Aizpurua, J.; Baumberg, J. J. Tracking Optical Welding through Groove Modes in Plasmonic Nano-Cavities. *Nano Lett.* **2016**, *16*, 5605.

- (22) Brown, L. V.; Sobhani, H.; Lassiter, J. B.; Nordlander, P.; Halas, N. J. Heterodimers: Plasmonic Properties of Mismatched Nanoparticle Pairs. *ACS Nano* **2010**, *4*, 819.

- (23) Slaughter, L. S.; Wu, Y.; Willingham, B. A.; Nordlander, P.; Link, S. Effects of Symmetry Breaking and Conductive Contact on the Plasmon Coupling in Gold Nanorod Dimers. *ACS Nano* **2010**, *4*, 4657.

- (24) Schubert, O.; Becker, J.; Carbone, L.; Khalavka, Y.; Provalskas, T.; Zins, I.; Sönnichsen, C. Mapping the Polarization Pattern of Plasmon Modes Reveals Nanoparticle Symmetry. *Nano Lett.* **2008**, *8*, 2345.

- (25) Crow, M. J.; Seekell, K.; Wax, A. Polarization Mapping of Nanoparticle Plasmonic Coupling. *Opt. Lett.* **2011**, *36*, 757.

- (26) Bhasikuttan, A. C.; Pal, H.; Mohanty, J. Cucurbit[n]uril Based Supramolecular Assemblies: Tunable Physico-Chemical Properties and Their Prospects. *Chem. Commun.* **2011**, *47*, 9959.
- (27) Chuntunov, L.; Haran, G. Trimeric Plasmonic Molecules: The Role of Symmetry. *Nano Lett.* **2011**, *11*, 4503.
- (28) Tian, X.; Zhou, Y.; Thota, S.; Zou, S.; Zhao, J. Plasmonic Coupling in Single Silver Nanosphere Assemblies by Polarization-Dependent Dark-Field Scattering Spectroscopy. *J. Phys. Chem. C* **2014**, *118*, 13801.
- (29) Esteban, R.; Borisov, A. G.; Nordlander, P.; Aizpurua, J. Bridging Quantum and Classical Plasmonics with a Quantum-Corrected Model. *Nat. Commun.* **2012**, *3*, 825.
- (30) Prodan, E.; Nordlander, P.; Halas, N. J. A Hybridization Model for the Plasmon Response of Complex Nanostructures. *Nano Lett.* **2003**, *3*, 1411.
- (31) Zhang, S.; Xu, H. Tunable Dark Plasmon in Metallic Nanocube Dimer: Toward Ultimate Sensitivity Nanoplasmonic Sensors. *Nanoscale* **2016**, *8*, 13722.
- (32) Popp, P. S.; Herrmann, J. F.; Fritz, E. C.; Ravoo, B. J.; Höppener, C. Impact of the Nanoscale Gap Morphology on the Plasmon Coupling in Asymmetric Nanoparticle Dimer Antennas. *Small* **2016**, *12*, 1667.
- (33) Mertens, J.; Eiden, A. L.; Sigle, D. O.; Huang, F.; Lombardo, A.; Sun, Z.; Sundaram, R. S.; Colli, A.; Tserkezis, C.; Aizpurua, J.; Milana, S.; Ferrari, A. C.; Baumberg, J. J. Controlling Subnanometer Gaps in Plasmonic Dimers Using Graphene. *Nano Lett.* **2013**, *13*, 5033.
- (34) Merlein, J.; Kahl, M.; Zuschlag, A.; Sell, A.; Halm, A.; Boneberg, J.; Leiderer, P.; Leitenstorfer, A.; Bratschitsch, R. Nanomechanical Control of an Optical Antenna. *Nat. Photonics* **2008**, *2*, 230.
- (35) Fan, J. A.; Bao, K.; Lassiter, J. B.; Bao, J.; Halas, N. J.; Nordlander, P.; Capasso, F. Near-Normal Incidence Dark-Field Microscopy: Applications to Nanoplasmonic Spectroscopy. *Nano Lett.* **2012**, *12*, 2817.
- (36) Kang, H.; Jia, B.; Gu, M. Polarization Characterization in the Focal Volume of High Numerical Aperture Objectives. *Opt. Express* **2010**, *18*, 10813.
- (37) Johnson, P. B.; Christy, R. W. Optical Constants of the Noble Metals. *Phys. Rev. B* **1972**, *6*, 4370.
- (38) Garcia de Abajo, F. J.; Howie, A. Retarded Field Calculation of Electron Energy Loss in Inhomogeneous Dielectrics. *Phys. Rev. B: Condens. Matter Mater. Phys.* **2002**, *65*, 115418.
- (39) Hohenester, U.; Trueger, A. MNPBEM – A Matlab Toolbox for the Simulation of Plasmonic Nanoparticles. *Comput. Phys. Commun.* **2012**, *183*, 370.
- (40) Hohenester, U. Simulating Electron Energy Loss Spectroscopy with the MNPBEM Toolbox. *Comput. Phys. Commun.* **2014**, *185*, 194.
- (41) Waxenegger, J.; Truegler, A.; Hohenester, U. Substrates and Layer Structures. *Comput. Phys. Commun.* **2015**, *193*, 138.
- (42) Vandenbosch, G. A. E.; Van de Capelle, A. R. Mixed-Po Tential Integral Expression Formulation of the Electric Field in a Stratified Dielectric Medium- Application to the Case of a Probe Current Source. *IEEE Trans. Antennas Propag.* **1992**, *40*, 806.